

Two-dimensional borophene: In-plane hyperbolic polaritons in the visible spectral range

*Yaser Abdi**, *Masoud Taleb*, *Soheil Hajibaba*, *Mohsen Moayedi*, *Nahid Talebi**

Y. Abdi, S. Hajibaba, M. Moayedi,

Department of Physics, University of Tehran, 1439955961 Tehran, Iran

E-mail: y.abdi@ut.ac.ir

M. Taleb, N. Talebi

Institute of Experimental and Applied Physics, Kiel University, 24118 Kiel, Germany

E-Mail: talebi@physik.uni-kiel.de

Keywords: hyperbolic polaritons, visible range, anisotropic, borophene, two-dimensional

Abstract - Two-dimensional metals, such as graphene, have undergone extensive exploration, with graphene exhibiting a metallic response limited to the infrared spectral range. Overcoming the challenge of extending the electron mobility in two-dimensional metals to achieve plasmonic behaviors in the visible range necessitates innovative synthesis procedures. In this study, we showcase the successful realization of the phase of χ_3 borophene on diverse substrates using aluminum-based chemical vapor deposition. Leveraging first-principle density-functional theory alongside advanced deep-subwavelength cathodoluminescence spectroscopy, we reveal the extreme anisotropic response of this material in the visible range, transitioning from hyperbolic polaritonic to an elliptic wavefront. Our calculations substantiate the experimental findings, positioning borophene as an unprecedented candidate for the in-plane hyperbolic response in the visible range. These results open avenues for pioneering optoelectronic applications in the visible spectrum, particularly through the incorporation of borophene into hybrid metallic-semiconducting heterostructures.

1. Introduction

Extreme confinement of light and tailoring its coupling with matter are at the heart of advanced solid-state-based quantum technologies. Polaritons are quasiparticles formed by the strong interaction of photons with a matter excitation. In particular, various forms of polaritons in two-dimensional (2D) materials are attractive candidates for further tailoring strong light-matter interactions, due to the reduced attenuation and screening effects^{1,2}. Moreover, 2D materials

offer a great versatility in forming hybrid material platforms, flavoring quasi-particle interactions³⁻⁵ and enhanced confinement of the light due to their reduced dimensionality⁶.

In addition to tailoring the dimensionality, reducing the symmetry of the crystal structure of 2D materials lead to even more functionalities⁷. Extreme anisotropic responses that lead to hyperbolic isofrequency surfaces^{8,9} and directional propagation¹⁰ enable a stronger coupling to localized emitters^{11,12}, enhancing the Purcell factor of quantum emitters^{13,14}, and achieving superlens functionalities¹⁵. Several metamaterial concepts have been suggested and realized^{16,17} to enable the hyperbolic isofrequency surfaces in specific frequency ranges. Nevertheless, and parallel to the metamaterials research, a vast of natural materials have recently emerged that sustain hyperbolic polaritonic features. Bulk and surface phonon polaritons in different kinds of materials, including uniaxial crystals such as hexagonal boron nitride¹⁸⁻²⁰ as well as biaxial crystals such as α -MoO₃^{21,22}, have been demonstrated. Phonon-polaritons are naturally excited in the far infrared spectral range, not accessible to the present spectral range of single-photon emitters and quantum technological applications. Therefore, hyperbolic materials in the visible range²³ appear as better candidates for quantum-optical applications, such as coupling to defect centers in 2D materials and vacancy centers in diamond²⁴.

A few materials such as tetradymites have been recently explored due to their highly non-symmetric uniaxial crystal structure and have been shown to enable hyperbolic surface polaritons within the visible range²⁵⁻²⁷. However, biaxial and in-plane hyperbolic features within the visible range in a natural material were not reported up to now. Here, we demonstrate a truly two-dimensional material, borophene, that features the excitation of in-plane hyperbolic polaritons.

Borophene have recently attracted several attentions, after the first synthesis of this material on a bulk metal^{28,29}. It has been demonstrated as a prototype of synthetic 2D materials development, without having a van der Waal bulk counterpart³⁰. It has been shown theoretically in 1990 that several classes of boron sheets should support free conduction electrons and behave as a metal³¹. More recently, borophene was suggested to enable a plasmonic response within the visible range, thanks to the high-mobility conduction electrons that this material sustains³². However, the optical response of free-standing borophene sheets, was not experimentally explored up to date, due to the previous synthesis methods used to enable a borophene sheet on an already existing bulk metal such as silver.

Here, using aluminum-assisted chemical vapor deposition, we realize borophene sheets in χ_3 phase on diverse substrate platforms^{33,34}. For investigating the optical properties of borophene, particularly it is favorable to realize free-standing borophene. We synthesize borophene on

holey-carbon transmission electron microscopy grids, and apply cathodoluminescence (CL) spectroscopy^{35,36} to explore the optical properties of borophene sheets, and explore its crystal structure using analytical transmission electron microscopy techniques as well as Raman spectroscopy. Using density-functional theory (DFT) based on Quantum ESPRESSO numerical codes, we further calculate the permittivity of single-layer borophene sheets. We further show, both theoretically and experimentally, that borophene enables extremely confined in-plane hyperbolic polaritons within the broad wavelength range of **521 nm** < λ < **1100 nm**, since the optics axis of this highly anisotropic crystal is placed oblique with respect to the normal to the sheet. Using CL spectroscopy, we further confirm the directionality of optical excitations in χ_3 borophene flakes. Our explorations, confirm that borophene is not only a 2D metal within the visible range, but also features an extreme anisotropic response and highly directional hyperbolic polaritons within the visible spectral range. Therefore, we suggest borophene in applications that enable strong interactions with highly confined quantum emitters and tailoring the radiation from such emitters.

2. In-plane Polaritons in Borophene

Our synthesis method that allows us to realize χ_3 borophene on arbitrary substrates will be discussed below. Here, we first discuss the main features that are expected from the extreme asymmetric crystal structure of single-layer borophene sheets. The structure of the χ_3 borophene consists of mixed triangular and hexagonal motifs, showing two in-plane principal axes along the directions shown by x and y arrows (perpendicular to each other) (see Figure 1b). The third principal axis along the z -direction is normal to the in-plane principal axes. χ_3 consists of atomic ribbons along the y direction, forming a multi-layer structure along the x -axis, similar to a macroscopic grating-like structure of parallel graphene ribbons with hyperbolic properties³⁷. Calculated permittivity of the χ_3 borophene sheets indeed demonstrates the extreme anisotropic response of the material (see Figure 1a): whereas the permittivity along the principal axis x features a dielectric response, the response along the y -axis is Drude metallic with the plasma wavelength located at $\lambda_p = \mathbf{521\ nm}$ ($E_p = \mathbf{2.38\ eV}$). DFT calculations in our work are performed using Quantum ESPRESSO³⁸. The electron-ion interaction is described with the optimized norm-conserving Vanderbilt pseudopotential³⁹. The exchange and correlation energies are described using the generalized gradient approximation (GGA) based on the approach of Perdew-Burke-Ernzerhof (PBE)⁴⁰. In all calculation, the plane wave cut-off energy is 50 Hartree. The relaxation was carried out with an $\mathbf{8 \times 8 \times 1}$ k-point mesh and a force threshold of $\mathbf{10^{-5}}$. We perform the calculation of the dielectric tensor through

the following sequential steps: first, we perform the initial self-consistent field (SCF) calculation by employing an $\mathbf{8} \times \mathbf{8} \times \mathbf{1}$ k-point mesh and including 16 bands. Subsequently, we conducted a more refined calculation using a finer $\mathbf{32} \times \mathbf{32} \times \mathbf{1}$ k-point mesh and 1000 bands for the non-self-consistent field (NSCF) calculation. Finally, a post-processing (PP) step was executed to obtain the dielectric tensor.

The Drude-like materials permittivity along the y direction next to the dielectric response along the x direction, comprises two domains for the optical response of the material. Within the wavelength range of $\lambda > \lambda_p$, the in-plane isofrequency surfaces of the material demonstrate type II hyperbolic features, whereas for the wavelengths $\lambda < \lambda_p$, the isofrequency surfaces have elliptical forms (see Figure 1c). Note, that the wavenumbers are complex-valued, demonstrating a nonvanishing attenuation of the optical waves confined to the borophene sheets with their propagation direction lying in the x - y plane.

We further examine the possibility for the propagation of in-plane polaritons in the borophene sheet. For highly anisotropic and particularly hyperbolic materials, several forms of bulk¹⁸, surface⁴¹, edge²⁶, and ghost⁴² polaritons have been already demonstrated in the literature. For all these polaritonic forms, even in the form of confinement to the surface, the material flakes should consist of a certain thickness, to be able to afford the propagation of hyperbolic polaritons. For an atomically thin material like borophene, in-plane hyperbolic polaritons can be better captured by considering a vanishing thickness for the material. Therefore, we translate the permittivity along x and y components into the in-plane conductivity tensor $\hat{\sigma}$, as $\hat{\sigma} = -i\omega d \hat{\varepsilon}$, where $\hat{\varepsilon}$ is the in-plane permittivity tensor and d is the thickness of the borophene film⁴³. As shown in the Supplementary Information Note 1, the spatial distributions associated with the field components of in-plane polaritons, for the borophene sheet located at $z = 0$ plane is constructed as $\psi(\vec{r}_{\parallel}, z) = \psi_0 \exp(-\kappa_z |z|) \exp(i\vec{k}_{\parallel} \cdot \vec{r}_{\parallel})$, with $\kappa_z^2 = k_{\parallel}^2 - k_0^2$ and $\vec{k}_{\parallel} = k_{\parallel} \cos \varphi \hat{x} + k_{\parallel} \sin \varphi \hat{y}$ and $\vec{r}_{\parallel} = x\hat{x} + y\hat{y}$ (see the inset of Figure 1d). Applying the boundary conditions, one obtains:

$$\kappa_z = \frac{k_0^2}{4i\omega(\sigma_{yy} \sin^2 \varphi + \sigma_{xx} \cos^2 \varphi)} \left\{ -\left(\frac{4}{\varepsilon_0} + \frac{\sigma_{xx}\sigma_{yy}}{\mu_0} \right) \pm \sqrt{\left(\frac{4}{\varepsilon_0} + \frac{\sigma_{xx}\sigma_{yy}}{\mu_0} \right)^2 - 16c^2 (\sigma_{yy} \sin^2 \varphi + \sigma_{xx} \cos^2 \varphi) (\sigma_{xx} \sin^2 \varphi + \sigma_{yy} \cos^2 \varphi)} \right\}, \quad (1)$$

where $k_0 = \omega/c$ is the free-space wavenumber, ε_0 and μ_0 are the free-space permittivity and permeability, respectively, ω is the angular frequency and c is the speed of light in vacuum. φ is the angle of the wave vector of the in-plane polaritons with respect to the principal axis x .

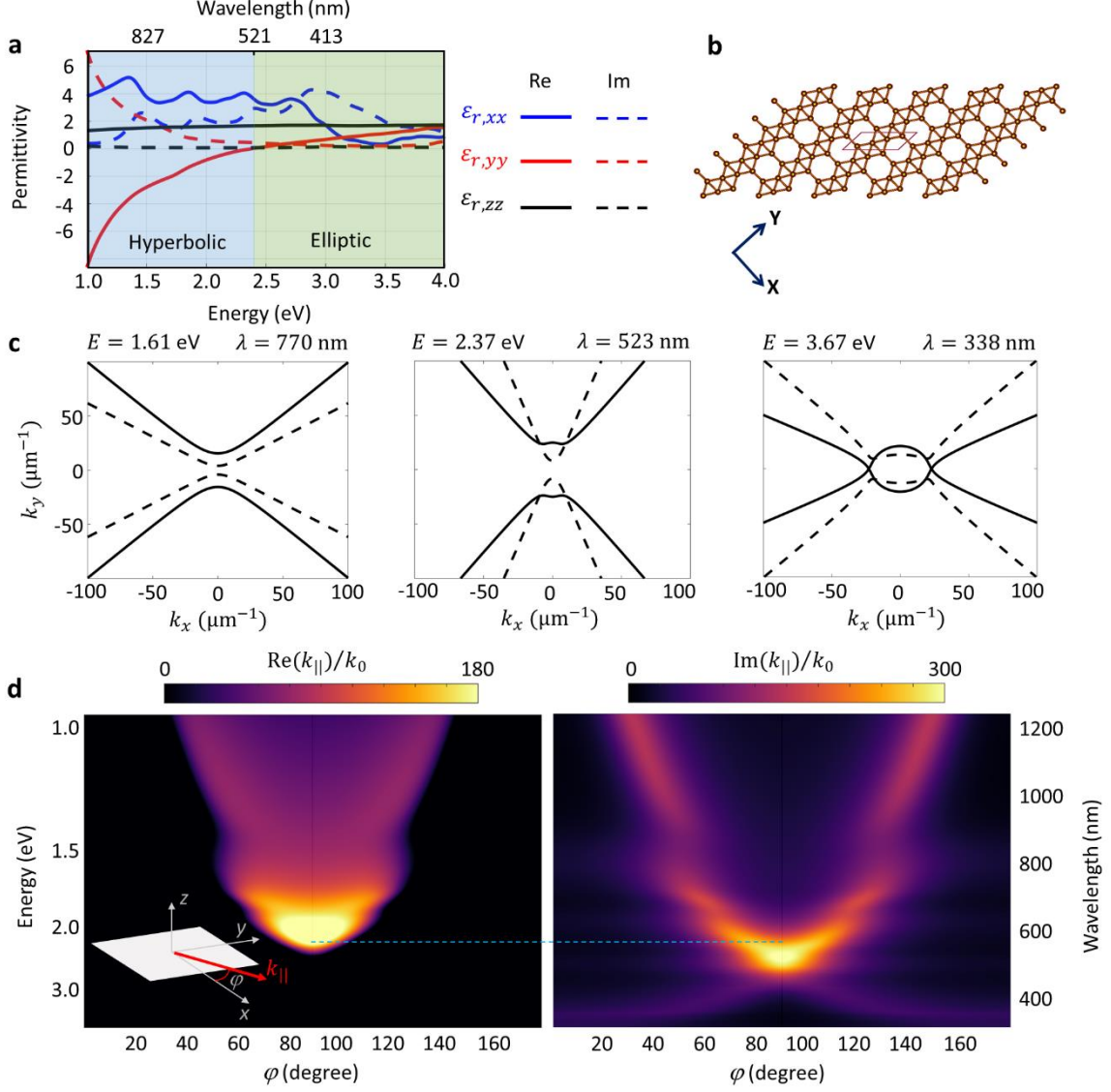


Figure 1. Biaxial hyperbolic electromagnetic responses of a Borophene flake. (a) Real and imaginary parts of the dielectric functions along the three principal axes. Shaded regions demonstrate the photon energy ranges where the optical responses show anisotropic hyperbolic and Elliptic characteristics. (b) Schematic of the crystalline Borophene monolayer in the x - y plane. (c) In-plane (x - y) iso-frequency surfaces at three depicted energies (wavelengths), showing the transition from in-plane hyperbolic to elliptic responses. Solid and dashed lines denote $\text{Re}\{k_y(k_x)\}$ and $\text{Im}\{k_y(k_x)\}$ respectively. (d) Propagation constant of the in-plane polaritons versus the azimuthal angle with respect to the principal axis x . (Left) Phase constant and (Right) attenuation constant. Blue dashed line is inserted as a guide for distinguishing the phase and attenuation constants associated with $\lambda = 600$ nm and $\varphi = 90^\circ$.

Using equation (1), the propagation constant of in-plane polaritons are obtained as $k_{||} = \sqrt{\kappa_z^2 + k_0^2}$.

The real part of $k_{||}$, which features the phase constant of polaritons in borophene, has a non-

zero value for only a specific range of angular distributions. This fact confirms the directional propagation of hyperbolic polaritons. Particularly along the x -axis the borophene sheet cannot sustain any form of interface modes, as expected. In contrast, the largest phase constant occurs for polaritons propagating along the y -axis at the wavelength of 600 nm ($E = 2.06$ eV), where the permittivity of the material along the y -axis is $\epsilon_{r yy} \approx -1$. At longer wavelengths, in-plane polaritons demonstrate an optimum directional propagation at an angle different from $\varphi = 90^\circ$, as shown in Figure 1d.

2.2. Synthesis of Borophene and Its Atomic Structure

To grow borophene sheets, the experiment starts with cleaning a (100) silicon wafer using RCA-1 solution which is a mixture of 5 parts deionized water, including 1 part ammonium hydroxide (27%) and 1 part hydrogen peroxide (30%). Next, a 100 nm-thick layer of aluminum (Al) is deposited on the cleaned wafer by physical vapor deposition at a base pressure of 3×10^{-6} Torr. The Al-coated silicon wafers are then placed in a chemical vapor deposition (CVD) chamber for the growth of borophene sheets. The CVD chamber is vacuumed to a pressure of 3×10^{-3} Torr and then the sample is annealed for 1 h at a temperature of 600 °C with a continuous flow of 20 sccm of H_2 gas. Growth of borophene begins by introducing a gas mixture of 15 sccm B_2H_6 (diborane) and 40 sccm H_2 into the CVD chamber. After 10 minutes, the flow of diborane is stopped and the sample is cold down to the room temperature over a period of 3 h in an H_2 ambient atmosphere. The growth of 2D borophene sheets concludes with the sheets growing on the substrate and being surrounded by aggregated Al islands (see Figure 2a). The mechanism of growth has been previously reported in detail³³.

To avoid substrate effects on the plasmonic behavior of borophene and remove Al aggregates, the as-grown borophene sheets are transferred onto a transmission electron microscopy copper grid. To transfer the sheets, first, poly methyl methacrylate (PMMA) is spin coated on the borophene/silicon sample (Fig 2b). Then the sample heated at 360 K for 5 minutes to ensure good adhesion of the borophene sheets to the PMMA. After heating, the PMMA-coated sample is immersed into hydrochloric acid for a few seconds to remove Al aggregations. The sample is then dipped into the DI water and these two steps are repeated to separate the PMMA from the substrate and remove the Al aggregates completely. After repeating this process a few times, the substrate is sunk into the DI water while the PMMA/borophene layer remains floating, as shown in Figure 2c. Finally, the layer is transferred onto the copper grid (Figure 2d) by dip coating, and the PMMA is removed by acetone (Figure 2e). The borophene sheets are left isolated onto copper grid and ready for cathodoluminescence measurements (Figure 2f).

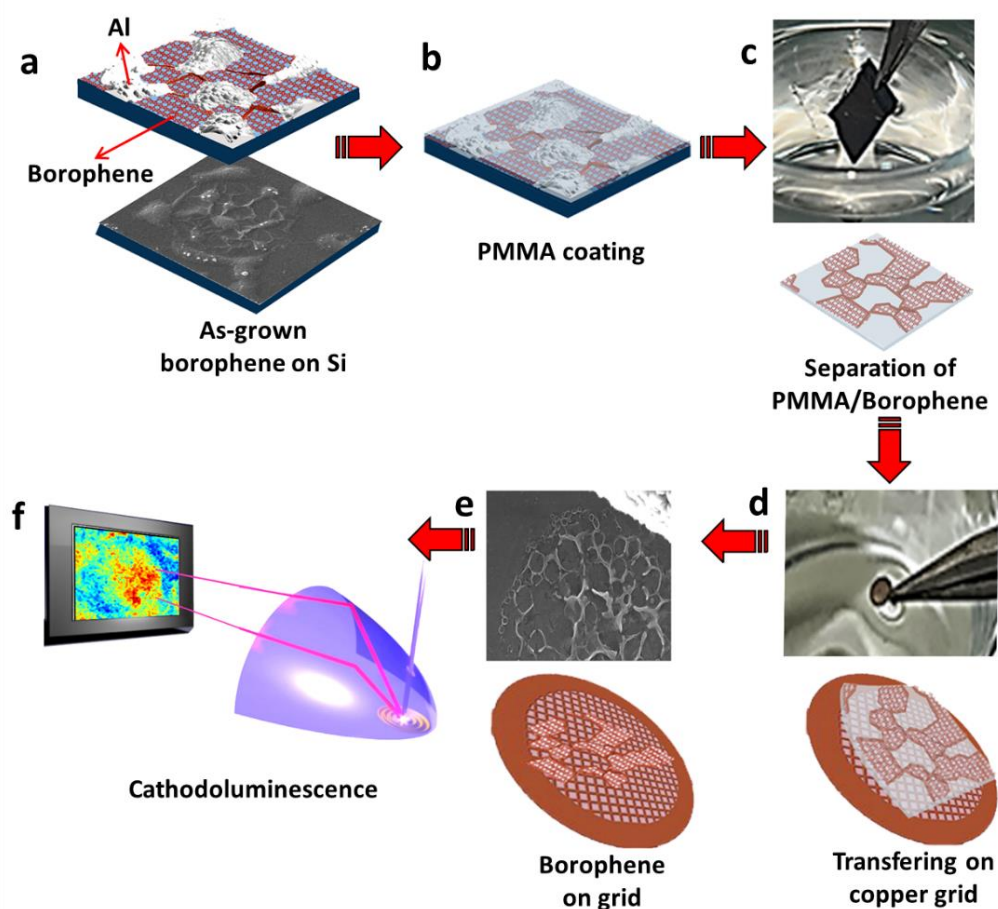


Figure 2. Schematical illustration of the synthesis process. (a) The bottom image shows a SEM image of as-grown borophene sheets on a silicon substrate. The top image shows the schematic of the same sample with white islands (bright area shown in SEM) representing Al aggregations and the grown sheets between the Al islands representing borophene. (b) PMMA (Poly methyl methacrylate) is coated on the sample. (c) PMMA-coated borophene is separated from the substrate and Al aggregates are removed using the transfer method explained in the text. (d) Floated PMMA/borophene is transferred onto a copper grid by fishing. (e) SEM (top) and schematic (bottom) images of borophene coated grid after removing the PMMA. (f) The schematic shows the cathodoluminescence setup.

Figure 3 presents structural and morphological analyses of borophene sheets. Figure 3a shows a scanning electron microscope (SEM) image of as-grown borophene on silicon substrate. The growth of borophene is based on an Al-based CVD approach, as mentioned above. Consequently, partial Al aggregates remain on the substrate at the end of the growth process. The bright bumps in the SEM image of Figure 3a are Al aggregates, and the borophene sheets grow between them. The wrinkles shown in this figure belong to the borophene sheets. Figure 3b displays SEM image of borophene sheets transferred onto a copper grid. The transferring step removes Al aggregates. The raised boundaries visible in the image are formed when the

borophene sheets meet each other during growth. Borophene sheets grown using this approach exhibit varying thicknesses. The sheets located between the Al aggregates, which are indicated in Figure 3c by a dashed enclosed line, are mostly monolayer borophene. A statistical investigation of the borophene sheets collected over various sheets by atomic force microscopy (AFM) also confirms the formation of 2- and 3-layer borophene sheets in this area. However, thicker sheets form in only specific parts of the sample, which are shown in Figure 3c by arrows. On the Al aggregates, some bright crystal-shaped structures are thicker borophene sheets. Additionally, the thicker borophene sheets grow at the boundaries of monolayer sheets (see the inset of Figure 3c).

The transferred borophene sheets on copper grid were characterized by high-resolution transmission electron microscopy (HRTEM). The images are shown in Figures 3d, and 3f, and the corresponding selected area electron diffraction (SAED) pattern is represented in Figure 3f. We observe an excellent consistency between the diffraction pattern we obtained and the primary reciprocal lattice of χ_3 borophene. The Miller indices corresponding to the observed diffraction pattern are included in this figure. We determine these Miller indices by comparing the theoretical values of the d – spacing with a standard deviation of 0.005. The HRTEM image of Figure 3d shows the parallel lattice strips with an interstrip distance of 4.4 and 2.1 angstroms, which is in excellent agreement with the distance between parallel strip-like regions of high atomic concentration and the atomic distance in the χ_3 phase, respectively. The magnified view of the HRTEM, along with the superimposed χ_3 borophene atomic structure, is included in the inset of the figure. The surface topography of the samples was investigated using an atomic force microscope (AFM). The resulting AFM images are presented in Figure 3g and 3h. Aluminum islands and borophene sheets with polygonal geometry can be distinguished from these figures. The distinctive sharp edges visible in the images correspond to the boundaries where borophene sheets have grown from different sides and seamlessly merged.

The Raman spectra of borophene reveal fascinating insights into its structural characteristics. The Raman fingerprints of the sample are represented in Figure 3i. The peaks around 180, 255, 305, 415, and 445 cm^{-1} are in good agreement with the B_g^2 , $B_g^2(X')$, $A_u(Y)$, B_g^1 , and $B_g^1(Y)$ mods, respectively, which were theoretically predicted for the χ_3 phase⁴⁴. Additionally, modes related to the presence of aluminum oxide (at 380 cm^{-1}) and the silicon substrate (at around 520 cm^{-1}) were also detected within the Raman spectrum. Furthermore, a peak at around 120 cm^{-1} serves as a signature of χ_3 phase, which has been previously observed in experiments³³.

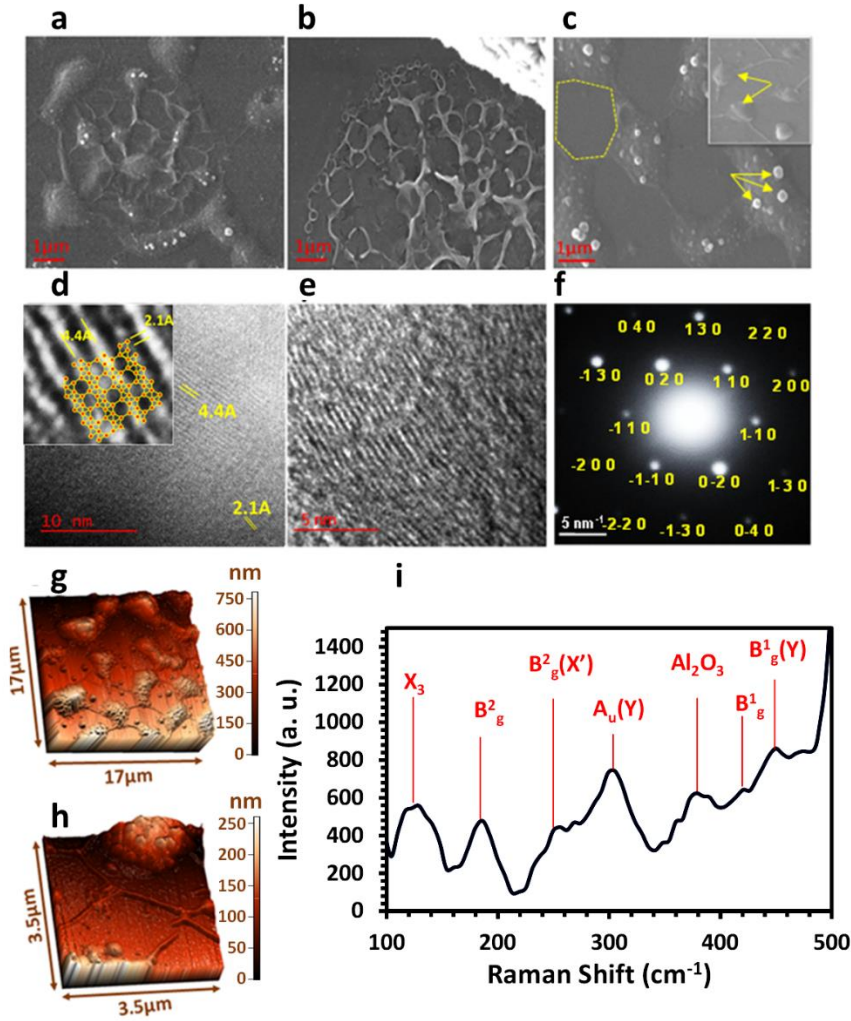


Figure 3. Morphological and structural analyses. (a) SEM image of as-grown borophene sheets on a silicon substrate. (b) SEM image of borophene on a copper grid. (c) SEM image showing the thicker sheets forming in some parts of the sample, which are indicated by arrows. (d) HRTEM image of borophene sheets showing the parallel lattice strips with interstrip distance of 4.4 and 2.1 angstroms which is in excellent agreement with the distance between parallel strip like regions of high atomic concentration and atomic distance in the χ_3 sheet, respectively. (d, e) HRTEM and (f) corresponding SADP of borophene which are well-matched with the crystal structure of the χ_3 phase. (g) AFM topographic image of as-grown borophene on Si showing the Al aggregates and borophene sheets between them. The polygon shape and sharp edges of the borophene domains suggests a crystalline structure. (h) AFM Magnified view of $3.5 \times 3.5 \mu\text{m}^2$. (i) Far-field Raman spectrum of borophene sheets.

2.3. Cathodoluminescence Spectroscopy of In-Plane Hyperbolic Polaritons in Borophene

To explore the optical response of borophene flakes, we use here CL spectroscopy, that allows us to reveal the spatio-spectral features of propagating⁴⁵⁻⁵¹ and localized⁵²⁻⁵⁶ polaritons in nano-structured samples. In our experimental scheme, the photons generated from the interaction

between the electron beam and borophene flakes are collected using a parabolic mirror and directed toward our analyzing path (Figure 4a). We perform spectroscopy, angle-resolved mapping, and polarimetry, to unravel the characteristics of localized hyperbolic polaritons in the synthesized borophene flakes. Our CL detector and optical analyzers are integrated with a Zeiss-SIGMA field-emission scanning electron microscope (SEM).

We first explore the CL response of single-layer borophene sheets that are formed into circular-like flakes with boundaries caused via the accumulation of the aluminum and borophene multi-layered structures (see the secondary electron SEM image, Figure 4b). This structural form allows for the formation of localized hyperbolic polaritons, occurring due to the interaction of the propagating hyperbolic polaritons with the boundaries of the flake and partial reflection from the boundaries. The averaged CL signal integrated over the wavelength range of 490 nm to 910 nm, demonstrates that the maximum detected photon yield originates from the borophene sheet, rather than the aluminum structure accumulated at the boundaries, and is caused by the excitation of hyperbolic in-plane polaritons.

Due to the directional propagation of hyperbolic polaritons, the spatial distribution of localized polaritons reflected from the boundaries does not entirely follow the morphology of the flake. At $\lambda = 500 \text{ nm}$, borophene does not support in-plane hyperbolic polaritons (see Figure 1d and the discussions therein). At this wavelength, the spatial position of the maximum CL signal originates from the accumulated aluminum rather than the borophene sheet. By increasing the wavelength and at $\lambda \geq 550 \text{ nm}$, in-plane hyperbolic polaritons are excited in the borophene flake, and particularly at longer wavelengths, the emerging localized polaritons demonstrate an elongated form highlighted by the black arrows (see the hyperspectral image at $\lambda = 800 \text{ nm}$). The propagation direction of in-plane hyperbolic polaritons at this wavelength is analytically derived to be $\varphi = 60^\circ$ with respect to the principal axis x and 30° with respect to the y -axis, allowing us to infer two possible orientations for the y -axis as shown in Figure 4c.

Figure 4d shows CL spectra acquired at selected electron impact positions marked in Figure 4b (right panel). We observe a rather broad spectral feature within the wavelength range 650 nm to 850 nm when the electron interacts with the borophene sheet. The absence of a sharp resonance is expected and is attributed to the presence of a large photonic density of state supported by the hyperbolic materials. The phase constant of in-plane hyperbolic polaritons at $\lambda = 800 \text{ nm}$ is approximately 100 times larger than the free-space wavenumber of the light, which means that in-plane polaritons should sustain an effective wavelength of approximately 8 nm at the wavelength range of 800 nm. This effect explains the absence of the standing-wave-like features in the hyperspectral CL images.

To better understand the characteristics of the optical response of borophene, we now consider a multilayer borophene structure, formed into a disc-like structure with the diameter of 350 nm (Figure 5a). CL spectra acquired from this structure show two broad spectral features, centered at the wavelengths of $\lambda = 577$ nm and $\lambda = 719$ nm. Hyperspectral images at these two wavelengths show the spatial distribution of the CL signal associated with two peaks. The optical resonance at $\lambda = 577$ nm demonstrate two maxima located at the outer rim of the structure along the y -axis. The lack of CL signal along the x -axis at this wavelength is due to the directional propagation of in-plane hyperbolic polaritons. Particularly at this wavelength, the direction of in-plane polaritons is along the y -principal axis (see Figure 1d), allowing us to determine the y -principal axis (and consequently also x -axis) without ambiguity (see the arrow depicted in Figure 5c, top).

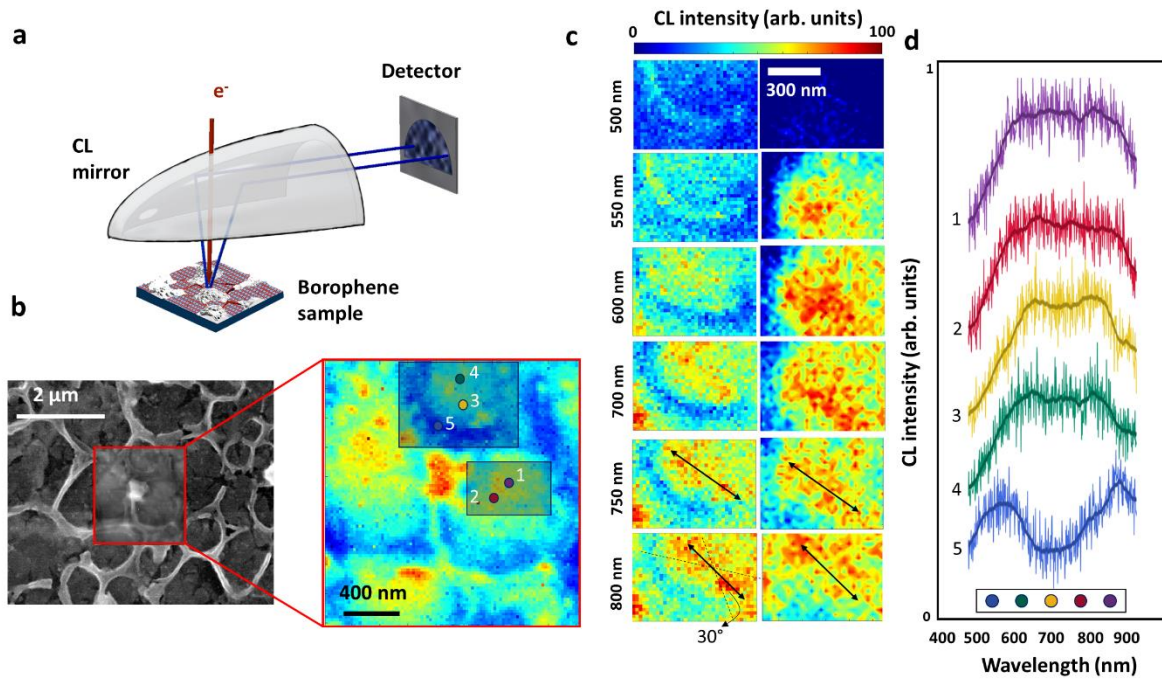


Figure 4. (a) Experimental setup featuring a CL mirror and the radiation emitted from the sample. (b) SEM image of the Borophene structure. The red square indicates the scanned area, while the adjacent image depicts average CL response. The black square within this hyperspectral image corresponds to the area analysed in panel, (c) revealing the spatial distribution of hyperbolic polaritons at selected wavelengths noted above each image. Black arrows on top of the image at $\lambda = 750$ nm and $\lambda = 800$ nm, demonstrate the orientation of in-plane plasmon propagation. Dashed lines demonstrate possible orientations for the y principal axis. (d) Spectrum extracted from the location marked by a red dot in panel (b).

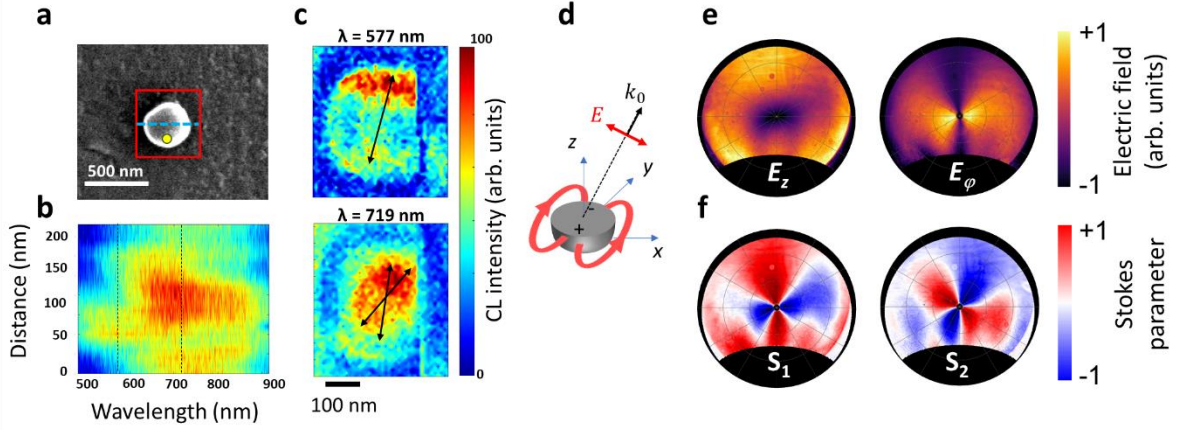


Figure 5. (a) Secondary-electron scanning Electron Microscopy image capturing a multilayer borophene flake (b) Distance-wavelength spectral distribution of CL light at the positions marked by the dashed cyan line in panel a. (c) Hyperspectral images of the particle at selected wavelengths (depicted above each image and marked by dashed line in panel (b), illustrating the localization of hyperbolic either at the rim along the y -axis or in the centre. (d) Excitation of a dipolar-like optical mode upon electron impact and far-field CL signal originated from this excitation. (e) E_z and E_φ components of the far-field electrical field distribution. (f) S_1 and S_2 Stokes parameters that are measured at $E = 1.55$ eV ($\lambda \approx 800$ nm) for the electron impact position shown in panel (a).

At the longer wavelength $\lambda = 719$ nm, in-plane polaritons propagate along two directions making an angle of 20° with respect to the y -axis. Due to the reflection of both these waves from the rim of the structure, the excited in-plane polaritons form a roundish pattern within the flake at this wavelength.

The coherent nature of the CL signal can be better determined by performing polarimetry. By acquiring the angular distribution of complete Stokes parameters, the angular pattern of the far-field radiation as well as the dipolar nature of the near-field resonance are retrieved (See Figure 5e). The z -component of the electric field demonstrates a donut-like shape, which is expected due to the transversal nature of the far-field radiation. The azimuthal component of the electric field demonstrates two lobes at $\varphi = 0$ and $\varphi = 180^\circ$, and zero intensities at $\varphi = \pm 90^\circ$. This behavior is attributed to the excitation of charges accumulated at rims along the y -axis, that further forms a dipolar resonance. Indeed, this interpretation is fully confirmed by analyzing the $S_1 = |E_x|^2 - |E_y|^2$ and $S_2 = 2\text{Re}\{E_x E_y^*\}$ stokes parameter, that demonstrate the excitation of a dipole along the y -axis (Figure 5f).

Conclusion

Here, we have explored the optical properties of synthesized free-standing borophene using deep-sub-wavelength cathodoluminescence spectroscopy. Using density functional theory, we have calculated the dielectric function along the principal axes and have shown that borophene is a so-far unique material platform for the excitation of in-plane hyperbolic polaritons in the visible range. In-plane hyperbolic polaritons in borophene demonstrate an extreme subwavelength feature, with an effective wavelength 180 times smaller than the wavelength of the free-space light at visible photon energies. We have analytically calculated the dispersion of in-plane hyperbolic polaritons that features a highly directional propagation mechanism, and further confirmed the excitation of hyperbolic polaritons using cathodoluminescence spectroscopy and polarimetry.

Extremely anisotropic hyperbolic polaritons have attracted a tremendous attention recently, after the discovery of hyperbolic polaritons in hBN and a few other non-symmetric crystals, all happening at the far infrared range. Our results establish borophene as the only material platform, so far, that supports in-plane hyperbolic polaritons in truly 2D materials and in the visible spectral range. Due to the impact of the hyperbolic response on tailoring the radiation from quantum emitters and manipulating the Purcell effect, borophene can be a material of choice for quantum-optical solid-state metrologies. In particular, when combined with deep-subwavelength characteristics of the in-plane polaritons in borophene, we anticipate that this 2D material can be used as well for manipulating the optical selection rules beyond dipole approximation, at the visible range. Similarly, Dirac plasmons in graphene have been theoretically suggested for tailoring the optical selection rules; however, at the far-infrared range⁵⁷. In addition, similar to graphene, this material could become an important candidate for light-driven electronic applications⁵⁸ and directional Schottky barrier in hybrid structures⁵⁹.

Supporting Information

Supporting Information is available from the Wiley Online Library or from the author.

Acknowledgements

Authors acknowledge fruitful discussions with Dr. Davoodi (Kiel University). This project has received funding from the European Research Council (ERC) under the European Union's Horizon 2020 research and innovation programme under grant agreement no. 802130 (Kiel, NanoBeam) and grant agreement no. 101017720 (EBEAM).

Received: ((will be filled in by the editorial staff))

Revised: ((will be filled in by the editorial staff))

Published online: ((will be filled in by the editorial staff))

References

- 1 Low, T. *et al.* Polaritons in layered two-dimensional materials. *Nature Materials* **16**, 182-194 (2017). <https://doi.org:10.1038/nmat4792>
- 2 Basov, D. N., Fogler, M. M. & García de Abajo, F. J. Polaritons in van der Waals materials. *Science* **354**, aag1992 (2016). <https://doi.org:doi:10.1126/science.aag1992>
- 3 Duong, D. L., Yun, S. J. & Lee, Y. H. van der Waals Layered Materials: Opportunities and Challenges. *ACS Nano* **11**, 11803-11830 (2017). <https://doi.org:10.1021/acsnano.7b07436>
- 4 Davoodi, F. *et al.* Tailoring the Band Structure of Plexcitonic Crystals by Strong Coupling. *ACS Photonics* **9**, 2473-2482 (2022). <https://doi.org:10.1021/acsp Photonics.2c00586>
- 5 Zhang, H. *et al.* Hybrid exciton-plasmon-polaritons in van der Waals semiconductor gratings. *Nature Communications* **11**, 3552 (2020). <https://doi.org:10.1038/s41467-020-17313-2>
- 6 Dubrovkin, A. M., Qiang, B., Krishnamoorthy, H. N. S., Zheludev, N. I. & Wang, Q. J. Ultra-confined surface phonon polaritons in molecular layers of van der Waals dielectrics. *Nature Communications* **9**, 1762 (2018). <https://doi.org:10.1038/s41467-018-04168-x>
- 7 Galiffi, E. *et al.* Extreme light confinement and control in low-symmetry phonon-polaritonic crystals. *Nature Reviews Materials* **9**, 9-28 (2024). <https://doi.org:10.1038/s41578-023-00620-7>
- 8 Poddubny, A., Iorsh, I., Belov, P. & Kivshar, Y. Hyperbolic metamaterials. *Nature Photonics* **7**, 948-957 (2013). <https://doi.org:10.1038/nphoton.2013.243>
- 9 Drachev, V. P., Podolskiy, V. A. & Kildishev, A. V. Hyperbolic metamaterials: new physics behind a classical problem. *Opt. Express* **21**, 15048-15064 (2013). <https://doi.org:10.1364/OE.21.015048>
- 10 Ni, X. *et al.* Observation of directional leaky polaritons at anisotropic crystal interfaces. *Nature Communications* **14**, 2845 (2023). <https://doi.org:10.1038/s41467-023-38326-7>
- 11 Newman, W. D. *et al.* Observation of long-range dipole-dipole interactions in hyperbolic metamaterials. *Science Advances* **4**, eaar5278 (2018). <https://doi.org:doi:10.1126/sciadv.aar5278>
- 12 Biehs, S. A., Menon, V. M. & Agarwal, G. S. Long-range dipole-dipole interaction and anomalous Förster energy transfer across a hyperbolic metamaterial. *Physical Review B* **93**, 245439 (2016). <https://doi.org:10.1103/PhysRevB.93.245439>
- 13 Poddubny, A. N., Belov, P. A., Ginzburg, P., Zayats, A. V. & Kivshar, Y. S. Microscopic model of Purcell enhancement in hyperbolic metamaterials. *Physical Review B* **86**, 035148 (2012). <https://doi.org:10.1103/PhysRevB.86.035148>
- 14 Jacob, Z., Smolyaninov, I. I. & Narimanov, E. E. Broadband Purcell effect: Radiative decay engineering with metamaterials. *Applied Physics Letters* **100** (2012). <https://doi.org:10.1063/1.4710548>
- 15 Liu, Z., Lee, H., Xiong, Y., Sun, C. & Zhang, X. Far-Field Optical Hyperlens Magnifying Sub-Diffraction-Limited Objects. *Science* **315**, 1686-1686 (2007). <https://doi.org:doi:10.1126/science.1137368>

- 16 Ferrari, L., Wu, C., Lepage, D., Zhang, X. & Liu, Z. Hyperbolic metamaterials and their applications. *Progress in Quantum Electronics* **40**, 1-40 (2015). <https://doi.org/https://doi.org/10.1016/j.pquantelec.2014.10.001>
- 17 Li, T. & Khurgin, J. B. Hyperbolic metamaterials: beyond the effective medium theory. *Optica* **3**, 1388-1396 (2016). <https://doi.org/10.1364/OPTICA.3.001388>
- 18 Dai, S. *et al.* Tunable Phonon Polaritons in Atomically Thin van der Waals Crystals of Boron Nitride. *Science* **343**, 1125-1129 (2014). <https://doi.org/doi:10.1126/science.1246833>
- 19 Caldwell, J. D. *et al.* Sub-diffractive volume-confined polaritons in the natural hyperbolic material hexagonal boron nitride. *Nature Communications* **5**, 5221 (2014). <https://doi.org/10.1038/ncomms6221>
- 20 Govyadinov, A. A. *et al.* Probing low-energy hyperbolic polaritons in van der Waals crystals with an electron microscope. *Nature Communications* **8**, 95 (2017). <https://doi.org/10.1038/s41467-017-00056-y>
- 21 Ma, W. *et al.* In-plane anisotropic and ultra-low-loss polaritons in a natural van der Waals crystal. *Nature* **562**, 557-562 (2018). <https://doi.org/10.1038/s41586-018-0618-9>
- 22 Zheng, Z. *et al.* A mid-infrared biaxial hyperbolic van der Waals crystal. *Science Advances* **5**, eaav8690 (2019). <https://doi.org/doi:10.1126/sciadv.aav8690>
- 23 High, A. A. *et al.* Visible-frequency hyperbolic metasurface. *Nature* **522**, 192-196 (2015). <https://doi.org/10.1038/nature14477>
- 24 Aharonovich, I., Englund, D. & Toth, M. Solid-state single-photon emitters. *Nature Photonics* **10**, 631-641 (2016). <https://doi.org/10.1038/nphoton.2016.186>
- 25 Esslinger, M. *et al.* Tetradymites as Natural Hyperbolic Materials for the Near-Infrared to Visible. *ACS Photonics* **1**, 1285-1289 (2014). <https://doi.org/10.1021/ph500296e>
- 26 Lingstädt, R. *et al.* Interaction of edge exciton polaritons with engineered defects in the hyperbolic material Bi₂Se₃. *Communications Materials* **2**, 5 (2021). <https://doi.org/10.1038/s43246-020-00108-9>
- 27 Talebi, N. *et al.* Wedge Dyakonov Waves and Dyakonov Plasmons in Topological Insulator Bi₂Se₃ Probed by Electron Beams. *ACS Nano* **10**, 6988-6994 (2016). <https://doi.org/10.1021/acsnano.6b02968>
- 28 Mannix, A. J. *et al.* Synthesis of borophenes: Anisotropic, two-dimensional boron polymorphs. *Science* **350**, 1513-1516 (2015). <https://doi.org/doi:10.1126/science.aad1080>
- 29 Feng, B. *et al.* Experimental realization of two-dimensional boron sheets. *Nature Chemistry* **8**, 563-568 (2016). <https://doi.org/10.1038/nchem.2491>
- 30 Mannix, A. J., Zhang, Z., Guisinger, N. P., Yakobson, B. I. & Hersam, M. C. Borophene as a prototype for synthetic 2D materials development. *Nature Nanotechnology* **13**, 444-450 (2018). <https://doi.org/10.1038/s41565-018-0157-4>
- 31 Boustani, I. New quasi-planar surfaces of bare boron. *Surface Science* **370**, 355-363 (1997). [https://doi.org/https://doi.org/10.1016/S0039-6028\(96\)00969-7](https://doi.org/https://doi.org/10.1016/S0039-6028(96)00969-7)
- 32 Dereshgi, S. A., Liu, Z. & Aydin, K. Anisotropic localized surface plasmons in borophene. *Opt. Express* **28**, 16725-16739 (2020). <https://doi.org/10.1364/OE.392011>
- 33 Mazaheri, A., Javadi, M. & Abdi, Y. Chemical Vapor Deposition of Two-Dimensional Boron Sheets by Thermal Decomposition of Diborane. *ACS Applied Materials & Interfaces* **13**, 8844-8850 (2021). <https://doi.org/10.1021/acsmami.0c22580>
- 34 Abdi, Y. *et al.* A Two-Dimensional Borophene Supercapacitor. *ACS Materials Letters* **4**, 1929-1936 (2022). <https://doi.org/10.1021/acsmaterialslett.2c00475>
- 35 Taleb, M., Davoodi, F., Diekmann, F. K., Rossnagel, K. & Talebi, N. Charting the Exciton–Polariton Landscape of WSe₂ Thin Flakes by Cathodoluminescence

- Spectroscopy. *Advanced Photonics Research* **3**, 2100124 (2022).
[https://doi.org:https://doi.org/10.1002/adpr.202100124](https://doi.org/10.1002/adpr.202100124)
- 36 Coenen, T. & Haegel, N. M. Cathodoluminescence for the 21st century: Learning
more from light. *Applied Physics Reviews* **4** (2017). [https://doi.org:10.1063/1.4985767](https://doi.org/10.1063/1.4985767)
- 37 Gomez-Diaz, J. S., Tymchenko, M. & Alù, A. Hyperbolic metasurfaces: surface
plasmons, light-matter interactions, and physical implementation using graphene strips
[Invited]. *Opt. Mater. Express* **5**, 2313-2329 (2015).
[https://doi.org:10.1364/OME.5.002313](https://doi.org/10.1364/OME.5.002313)
- 38 Giannozzi, P. *et al.* QUANTUM ESPRESSO: a modular and open-source software
project for quantum simulations of materials. *Journal of Physics: Condensed Matter*
21, 395502 (2009). [https://doi.org:10.1088/0953-8984/21/39/395502](https://doi.org/10.1088/0953-8984/21/39/395502)
- 39 Hamann, D. R. Optimized norm-conserving Vanderbilt pseudopotentials. *Physical
Review B* **88**, 085117 (2013). [https://doi.org:10.1103/PhysRevB.88.085117](https://doi.org/10.1103/PhysRevB.88.085117)
- 40 Ernzerhof, M. & Scuseria, G. E. Assessment of the Perdew–Burke–Ernzerhof
exchange–correlation functional. *The Journal of Chemical Physics* **110**, 5029-5036
(1999). [https://doi.org:10.1063/1.478401](https://doi.org/10.1063/1.478401)
- 41 Dai, S. *et al.* Manipulation and Steering of Hyperbolic Surface Polaritons in
Hexagonal Boron Nitride. *Advanced Materials* **30**, 1706358 (2018).
[https://doi.org:https://doi.org/10.1002/adma.201706358](https://doi.org/10.1002/adma.201706358)
- 42 Ma, W. *et al.* Ghost hyperbolic surface polaritons in bulk anisotropic crystals. *Nature*
596, 362-366 (2021). [https://doi.org:10.1038/s41586-021-03755-1](https://doi.org/10.1038/s41586-021-03755-1)
- 43 Pan, D., Yu, R., Xu, H. & García de Abajo, F. J. Topologically protected Dirac
plasmons in a graphene superlattice. *Nature Communications* **8**, 1243 (2017).
[https://doi.org:10.1038/s41467-017-01205-z](https://doi.org/10.1038/s41467-017-01205-z)
- 44 Sheng, S. *et al.* Raman Spectroscopy of Two-Dimensional Borophene Sheets. *ACS
Nano* **13**, 4133-4139 (2019). [https://doi.org:10.1021/acsnano.8b08909](https://doi.org/10.1021/acsnano.8b08909)
- 45 van Wijngaarden, J. T. *et al.* Direct imaging of propagation and damping of near-
resonance surface plasmon polaritons using cathodoluminescence spectroscopy.
Applied Physics Letters **88** (2006). [https://doi.org:10.1063/1.2208556](https://doi.org/10.1063/1.2208556)
- 46 Aharonovich, I. *et al.* Diamond-based single-photon emitters. *Reports on Progress in
Physics* **74**, 076501 (2011). [https://doi.org:10.1088/0034-4885/74/7/076501](https://doi.org/10.1088/0034-4885/74/7/076501)
- 47 Suzuki, T. & Yamamoto, N. Cathodoluminescent spectroscopic imaging of surface
plasmon polaritons in a 1-dimensional plasmonic crystal. *Opt. Express* **17**, 23664-
23671 (2009). [https://doi.org:10.1364/OE.17.023664](https://doi.org/10.1364/OE.17.023664)
- 48 Sannomiya, T. *et al.* Cathodoluminescence Phase Extraction of the Coupling between
Nanoparticles and Surface Plasmon Polaritons. *Nano Letters* **20**, 592-598 (2020).
[https://doi.org:10.1021/acs.nanolett.9b04335](https://doi.org/10.1021/acs.nanolett.9b04335)
- 49 Kuttge, M. *et al.* Loss mechanisms of surface plasmon polaritons on gold probed by
cathodoluminescence imaging spectroscopy. *Applied Physics Letters* **93** (2008).
[https://doi.org:10.1063/1.2987458](https://doi.org/10.1063/1.2987458)
- 50 Taleb, M. *et al.* Spin–orbit interactions in plasmonic crystals probed by site-selective
cathodoluminescence spectroscopy. *Nanophotonics* **12**, 1877-1889 (2023).
[https://doi.org:doi:10.1515/nanoph-2023-0065](https://doi.org/10.1515/nanoph-2023-0065)
- 51 Guo, S. *et al.* Far-Field Radiation of Three-Dimensional Plasmonic Gold Tapers near
Apexes. *ACS Photonics* **6**, 2509-2516 (2019).
[https://doi.org:10.1021/acsp Photonics.9b00838](https://doi.org/10.1021/acsp Photonics.9b00838)
- 52 Schilder, N. J., Agrawal, H., Garnett, E. C. & Polman, A. Phase-Resolved Surface
Plasmon Scattering Probed by Cathodoluminescence Holography. *ACS Photonics* **7**,
1476-1482 (2020). [https://doi.org:10.1021/acsp Photonics.0c00209](https://doi.org/10.1021/acsp Photonics.0c00209)

- 53 Gómez-Medina, R., Yamamoto, N., Nakano, M. & García de Abajo, F. J. Mapping plasmons in nanoantennas via cathodoluminescence. *New Journal of Physics* **10**, 105009 (2008). <https://doi.org:10.1088/1367-2630/10/10/105009>
- 54 Guo, S., Talebi, N. & van Aken, P. A. Long-Range Coupling of Toroidal Moments for the Visible. *ACS Photonics* **5**, 1326-1333 (2018). <https://doi.org:10.1021/acsphotonics.7b01313>
- 55 Guo, S., Talebi, N., Campos, A., Kociak, M. & van Aken, P. A. Radiation of Dynamic Toroidal Moments. *ACS Photonics* **6**, 467-474 (2019). <https://doi.org:10.1021/acsphotonics.8b01422>
- 56 Kociak, M. & Stéphan, O. Mapping plasmons at the nanometer scale in an electron microscope. *Chemical Society Reviews* **43**, 3865-3883 (2014). <https://doi.org:10.1039/C3CS60478K>
- 57 Machado, F., Rivera, N., Buljan, H., Soljačić, M. & Kaminer, I. Shaping Polaritons to Reshape Selection Rules. *ACS Photonics* **5**, 3064-3072 (2018). <https://doi.org:10.1021/acsphotonics.8b00325>
- 58 Higuchi, T., Heide, C., Ullmann, K., Weber, H. B. & Hommelhoff, P. Light-field-driven currents in graphene. *Nature* **550**, 224-228 (2017). <https://doi.org:10.1038/nature23900>
- 59 Campbell, J. C., Blum, F. A., Shaw, D. W. & Lawley, K. L. GaAs electro - optic directional - coupler switch. *Applied Physics Letters* **27**, 202-205 (2008). <https://doi.org:10.1063/1.88428>

Supporting Information

Two-dimensional borophene: In-plane hyperbolic polaritons in the visible spectral range

Y. Abdi, Soheil Hajibaba, Mohsen Moayedi,

Department of Physics, University of Tehran, 1439955961 Tehran, Iran

E-mail: y.abdi@ut.ac.ir

M. Taleb, N. Talebi

Institute of Experimental and Applied Physics, Kiel University, 24118 Kiel, Germany

E-Mail: talebi@physik.uni-kiel.de

Content:

- 1. In-plane polaritons in an atomically thin borophene sheet**

1. In-plane polaritons in an atomically thin borophene sheet

We consider a borophene sheet located at the $z=0$ plane, supporting in-plane surface waves confined to the plane and propagating along the direction specified by the azimuthal angle φ with respect to the principal axis x . We consider the vector potential approach allowing us to decompose the waves into transverse-magnetic (TM) and transverse-electric (TE) parts, by choosing $\vec{A} = (0, 0, A_z)$ and $\vec{F} = (0, 0, F_z)$, with \vec{A} and \vec{F} being the magnetic and electric vector potentials. Therefore, the z -components of the magnetic and electric vector potentials are constructed as

$$A_z(x, y, z) = \begin{cases} A_1 e^{-\kappa_z z} e^{ik_{\parallel} \cos \varphi x + ik_{\parallel} \sin \varphi y} & z > 0 \\ A_2 e^{+\kappa_z z} e^{ik_{\parallel} \cos \varphi x + ik_{\parallel} \sin \varphi y} & z < 0 \end{cases} \quad (\text{S1})$$

and

$$F_z(x, y, z) = \begin{cases} F_1 e^{-\kappa_z z} e^{ik_{\parallel} \cos \varphi x + ik_{\parallel} \sin \varphi y} & z > 0 \\ F_2 e^{+\kappa_z z} e^{ik_{\parallel} \cos \varphi x + ik_{\parallel} \sin \varphi y} & z < 0 \end{cases} \quad (\text{S2})$$

respectively. The electric and magnetic field components are obtained as

$$\vec{E}(x, y, z) = -\vec{\nabla} \times \vec{F} - \frac{1}{i\omega\epsilon_0} \vec{\nabla} \times \vec{\nabla} \times \vec{A} \quad (\text{S3})$$

and

$$\vec{H}(x, y, z) = \vec{\nabla} \times \vec{A} - \frac{1}{i\omega\mu_0} \vec{\nabla} \times \vec{\nabla} \times \vec{F}, \quad (\text{S4})$$

Respectively. Using equations (S1) to (S4) and applying the boundary conditions as

$\hat{z} \times (\vec{H}_1 - \vec{H}_2) = \hat{\sigma} : \vec{E}_{\parallel}$ and $\hat{z} \times (\vec{E}_1 - \vec{E}_2) = 0$, one obtains $A_1 = -A_2$ and $F_1 = F_2$, and the following relation between the A_i and F_i coefficients:

$$+ \left(2 - \sigma_{yy} \frac{\kappa_z}{i\omega\mu_0} \right) \sin \varphi A_1 = \cos \varphi \left(2 \frac{\kappa_z}{i\omega\epsilon_0} - \sigma_{yy} \right) F_1 \quad (\text{S5})$$

and

$$- \left(2 - \sigma_{xx} \frac{\kappa_z}{i\omega\mu_0} \right) \cos \varphi A_1 = \sin \varphi \left(2 \frac{\kappa_z}{i\omega\epsilon_0} - \sigma_{xx} \right) F_1 \quad (\text{S6})$$

Simultaneous satisfaction of equations (S5) and (S6) leads to the following values for the decay ratio κ_z :

$$\kappa_z = \frac{k_0^2}{4i\omega(\sigma_{yy} \sin^2 \varphi + \sigma_{xx} \cos^2 \varphi)} \left\{ - \left(\frac{4}{\epsilon_0} + \frac{\sigma_{xx} \sigma_{yy}}{\mu_0} \right) \pm \sqrt{\left(\frac{4}{\epsilon_0} + \frac{\sigma_{xx} \sigma_{yy}}{\mu_0} \right)^2 - 16c^2 (\sigma_{yy} \sin^2 \varphi + \sigma_{xx} \cos^2 \varphi) (\sigma_{xx} \sin^2 \varphi + \sigma_{yy} \cos^2 \varphi)} \right\}$$

as shown in the main text, as well as the following results for the in-plane components of the electric field:

$$E_\alpha = +A_1 \left\{ \frac{\kappa_z}{i\omega\mu_0} + \left(2 - \sigma_{\alpha\alpha} \frac{\kappa_z}{i\omega\mu_0} \right) \left(2 \frac{\kappa_z}{i\omega\varepsilon_0} - \sigma_{\alpha\alpha} \right)^{-1} \right\} (ik_\alpha) e^{-\kappa_z|z|} e^{i\vec{k}_\parallel \cdot \vec{r}_\parallel} \quad (\text{S7})$$

and the tangential components of the magnetic field represented as $\vec{H}_\parallel = \frac{1}{\eta_0} \hat{z} \times \vec{E}_\parallel$.